Scaling Relationship and Optimization of Double-Pulse Electroporation

Mohamed M. Sadik,[†] Miao Yu,[†] Mingde Zheng,[‡] Jeffrey D. Zahn,[‡] Jerry W. Shan,[†] David I. Shreiber,[‡] and Hao Lin[†*]

[†]Department of Mechanical and Aerospace Engineering and [‡]Department of Biomedical Engineering, Rutgers, The State University of New Jersey, Piscataway, New Jersey

ABSTRACT The efficacy of electroporation is known to vary significantly across a wide variety of biological research and clinical applications, but as of this writing, a generalized approach to simultaneously improve efficiency and maintain viability has not been available in the literature. To address that discrepancy, we here outline an approach that is based on the mapping of the scaling relationships among electroporation-mediated molecular delivery, cellular viability, and electric pulse parameters. The delivery of Fluorescein-Dextran into 3T3 mouse fibroblast cells was used as a model system. The pulse was rationally split into two sequential phases: a first precursor for permeabilization, followed by a second one for molecular delivery. Extensive data in the parameter space of the second pulse strength and duration were collected and analyzed with flow cytometry. The fluorescence intensity correlated linearly with the second pulse duration, confirming the dominant role of electrophoresis in delivery. The delivery efficiency exhibited a characteristic sigmoidal dependence on the field strength. An examination of short-term cell death using 7-Aminoactinomycin D demonstrated a convincing linear correlation with respect to the electrical energy. Based on these scaling relationships, an optimal field strength becomes identifiable. A model study was also performed, and the results were compared with the experimental data to elucidate underlying mechanisms. The comparison reveals the existence of a critical transmembrane potential above which delivery with the second pulse becomes effective. Together, these efforts establish a general route to enhance the functionality of electroporation.

INTRODUCTION

Electroporation-mediated molecular delivery is an effective means to manipulate cells in biological research and medical applications (1–5). In this method, cells are exposed to an applied electric field to transiently permeabilize the membrane, and facilitate the uptake of biologically active molecules into the cytoplasm. This physical delivery method has been applied widely in areas such as drug and gene delivery, protein insertion, and cancer therapy, among others (3–9).

Fundamental studies demonstrated that electroporation-mediated molecular delivery is affected by both membrane permeabilization and molecular transport into the cytoplasm (10–13). The pulsing parameters, cell size, and conductivity across the cellular membrane regulate the transmembrane potential that controls the degree of membrane permeabilization (14–24). The target molecules are transported through the permeabilized membrane into the cytoplasm, and the process depends on their size and charge. Molecules with larger size (MW $>$ 4 (25)) such as DNA rely mainly on electrophoresis and other membrane-DNA interactions, such as endocytosis, to traverse the cell membrane (1,12,24–27). Simple diffusion and electrophoresis mechanisms are speculated to control the transport of smaller molecules such as calcium, propidium iodide, Lucifer yellow, and most drug molecules (25,28–33).

Extensive research has been performed to improve electroporation (5,34–43). Various strategies have been employed, including the optimization of the electric field parameters (pulse shape (16,44–46), electric field pulse strength (37,39,47–49), and duration (25,50)), the electroporation media (buffer electrical conductivity (18,28,29,31,33,51)), osmolarity (52–54), and chemical composition (28,55–57)), and novel chip design (10,39,53,58–61). Of particular interest to this study is the first approach, namely, the exploration of the pulsing parameter space to enhance molecular delivery and viability. Earlier studies utilized single pulses with relatively high field strength (27,62) to perform both permeabilization and transport (26,42,63). Although an appreciable delivery can be achieved, a large portion of the permeabilized cells do not survive the electrical shock (37,38). To overcome this limitation, more elaborate pulsing designs have been used, including unipolar and bipolar pulses (45), alternating-current fields (64), non-square-wave forms (16), pulse trains (17,25,52,54,63), and a combination of pulses with high and low field strengths (denoted by "HV" and "LV", respectively) (27,62,65,66). Notably, an elaborate series of work by Puc et al. (32) and Pucihar et al. (67) resulted in the development of an optimization scheme for the delivery of small molecules and viability using single pulses, which was later complemented by a study revealing pulse parameters with equivalent permeabilization. Despite the progresses demonstrated by these attempts, the protocols and the corresponding approaches, due to their lack of generality, could not be readily translated into a widely applicable methodology.

Submitted July 24, 2013, and accepted for publication December 31, 2013.

*Correspondence: hlin@jove.rutgers.edu

Editor: Edward Stuenkel.

0006-3495/14/02/0801/12 $2.00

http://dx.doi.org/10.1016/j.bpj.2013.12.045

The main objective of this work is to identify a possible route for protocol optimization based on contemporary understanding of electroporation mechanisms. For this purpose, the combination of HV/LV pulses is attractive. This approach is based on the idea that permeabilization and transport can be treated as separate tasks, and can be accomplished by HV and LV, respectively. The application of the HV pulse is in general a necessary condition for membrane permeabilization, presumably to overcome the critical threshold of the transmembrane potential (27,66). On the other hand, once permeabilization is achieved, an LV can be employed to deliver the molecules effectively while simultaneously decreasing damage due to field exposure (27,65,66). This approach has been proven to be effective by many studies for the delivery of large molecules using different pulsing parameters such as HV and LV field strengths, their duration, and the delay between them. For example, Sukharev et al. (27) showed that extending the second pulse duration enhanced DNA uptake, which scales linearly with electrical charge. A series of studies by André and Mir (1), André et al. (66), and Bureau et al. (68) demonstrated the necessity of second pulses in delivering DNA in vivo. Using a control system for in vivo electroporation, Cukjati et al. (69) controlled the degree of permeabilization by adjusting the first pulse of the HV/LV sequence in real-time, and demonstrated that tissue complexity affected significantly the delivery efficiency. Kandušer et al. (65) used various combinations of HV/LV pulses that appreciably enhanced the relative transfection efficiency of eGFP plasmid vectors. Similar trends were observed by Stroh et al. (62) when eGFP plasmid vectors and siRNA were delivered to primary cells and different cell lines. These studies demonstrated that the use of HV/LV combination is a promising approach for enhancing delivery. However, important questions remain:

1. How do the HV/LV pulses quantitatively affect delivery, and do lower and higher bounds exist for effective delivery with the LV pulse?
2. How does viability scale with the field strength and duration of the LV pulse?
3. Is an optimal pulsing scheme identifiable to simultaneously enhance delivery and viability?

The answers to these questions will help us establish a generalized method that is based on scaling relationships among delivery, viability, and electric pulse parameters.

In this work, we begin to address these questions by systematically characterizing the scaling behavior of both delivery and (short-term) cell viability with respect to pulsing parameters in combined HV/LV electroporation. We used 3T3 mouse fibroblasts as a model cell. The applied first pulse had a relatively strong field strength (100,000 V/m) and a duration of 0.001 s. Without delay, a second pulse is applied with field strength and duration varying from 10,000 to 100,000 V/m and 0.01 to 0.1 s, respectively. The target molecule for delivery was Fluorescein-Dextran (FD), a chain polymer with a molecular weight of ~10,000. We chose this molecule due to its nonbinding nature, and its proximity in size to small RNA, peptides, and drug molecules (12,25,50,70). Cellular viability was assayed using 7-Aminoactinomycin D (7-AAD). The data were collected with high-throughput fluorescence-based flow cytometry for a statistically significant number of cells (10,000) to construct a comprehensive mapping of delivery and viability (37,47,62,70). These results allow us to analyze the system behavior extensively, from which an optimization scheme emerges. In addition, we also compare the experimental results to a whole-cell level transport model that quantitatively predicted both membrane permeability and FD delivery. The comparison provides mechanism-based interpretations of the experimental data. The combined efforts establish a general methodology for the improvement of electroporation as a delivery technique: a systematic optimization can be pursued if these scaling relationships become available.

MATERIALS AND METHODS

Cell culture

NIH 3T3 mouse fibroblast cells were cultured in Dulbecco's Modified Eagle Medium supplemented with Fetal Bovine Serum (10% v/v), Penicillin-Streptomycin (1% v/v), and L-Glutamine (1% v/v) (Sigma-Aldrich, St. Louis, MO) at 37°C and 5% CO_2. Before each experiment, cells were harvested at 70–80% confluency using 0.5% trypsin/EDTA (Sigma-Aldrich) and washed with culture media. The cell suspension was spun for 2 min at 460×g (2000 rpm) (Allegra X-21; Beckman Coulter, Brea, CA) and washed with the electroporation buffer containing 0.5 mM $MgCl_2$, 200 mM sucrose, and 10 mM HEPES (Sigma-Aldrich) (pH 7.4) (33). The electrical conductivity (CON 6; Oakton Instruments, Vernon Hills, IL) and osmolality (3D3 Osmometer; Advanced Instruments, Norwood, MA) of the electroporation buffer were 100 μS/cm and 310 mOsm/kg, respectively (11,33).

Electroporation protocol

Approximately 3×10^6 cells/mL were suspended in the electroporation buffer containing 100 μM of Fluorescein-Dextran (FD; Life Technologies, Grand Island, NY) and incubated on ice for 5 min before pulsation. The physical properties of FD are listed in Table 1 (ex: 494 nm, em: 524 nm). The electroporation experiments were conducted at room temperature (20°C) under a sterile hood. A volume of 90 μL of cell suspension was placed into an electroporation cuvette (model No. 89047-206; VWR, Philadelphia, PA). The cuvette was made from polycarbonate material with electrodes made from polished aluminum plates. The spacing between the electrodes was 1 mm. For each data point, one new cuvette is used. Various combinations of double pulses were applied using a custom-built electroporator that can deliver calibrated and controlled square pulses (Fig. 1). The first pulse was programmed at V_1 = 100 V (E_1 = 100,000 V/m) and t_1 = 0.001 s in strength and duration at all times, respectively. This pulse has been shown to promote significant permeabilization with low delivery and high viability trend for different cell and molecule types (24,25,32,38,47,48,71). Our own experiments using the same field strength and varying durations also confirm this trend (data not shown). Ten voltages were used for the second pulse, namely, 10, 20, 25, 30, 35, 40, 50, 60, 80, and 100 V to achieve electric field strengths (E_2) between

TABLE 1 List of model parameters

Symbol	Definition	Value
a	Cell radius	7 μm (33)
h	Membrane thickness	5 nm
σ_i	Intracellular conductivity	0.4 S/m (28,31)
σ_e	Extracellular conductivity	0.01 S/m
F	Faraday constant	96,485 C/mol
R	Universal gas constant	8.314 J/K · mol
T	Room temperature	298.15 K
$D_{FD,i}$	Diffusion coefficient of FD in the cytoplasm	2.90×10^{-11} m^2/s (73,74)
$D_{FD,e}$	Diffusion coefficient of FD in the extracellular solution	9.80×10^{-11} m^2/s (75)
z_{FD}	Net charge of FD	−0.1 (73,74)
$[FD]_{i,o}$	Initial FD concentration in the cytoplasm	0 M
$[FD]_{e,o}$	Initial FD concentration in the extracellular solution	100 μM
E_1	Applied electric field strength of first pulse	100,000 V/m
E_2	Applied electric field strength of second pulse	10,000–100,000 V/m
t_1	Applied electric field duration of first pulse	0.001 s
t_2	Applied electric field duration of second pulse	0.01–0.1 s

If reference is not given, value is from this article. FD denotes Fluorescein-Dextran.

10,000 and 100,000 V/m. (Note that although we follow the conventional terminology of HV/LV, for the purpose of parametric study, some of our second-pulse strengths are approaching that of the first one and are no longer considered low.) The duration of the second pulse (t_2) was varied between 0.01 and 0.1 s. At postpulsation, the cell suspension was incubated in complete media for a 15-min period to allow membrane resealing (37,38,72). To remove free FD, cells were washed twice with phosphate-buffered saline Mg^{2+} and Ca^{2+} for 2 min at 460×g (2000 rpm) each (Sigma-Aldrich). The cells were incubated for another 15 min, then resuspended in phosphate-buffered saline containing 2 μM of 7-Aminoactinomycin D (7-AAD, 1270.43 Da; Life Technologies), a membrane-impermeant dye that fluoresces upon binding to DNA (ex: 488 nm, em: 650 nm) to identify nonviable cells that failed to reseal. Both FD and 7-AAD fluorescence signals were acquired using flow cytometry 2 h after the addition of 7-AAD. For these experimental conditions and using a simplified model, the temperature change due to Joule heating was estimated to be 2.5°C in the worse-case scenario.

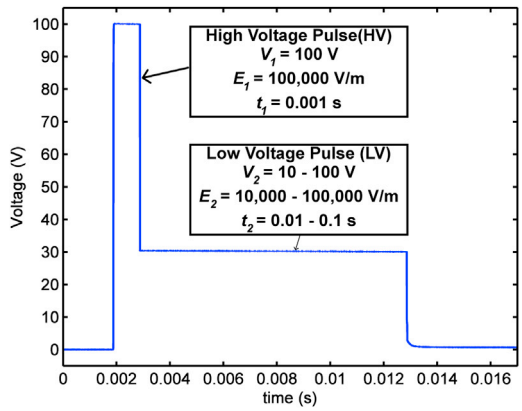

FIGURE 1 An exemplary double pulse used in the delivery of Fluorescein-Dextran into 3T3 mouse fibroblasts. The first pulse was 100,000 V/m in strength and 0.001 s in duration. The second pulse was 30,000 V/m in strength and 0.01 s in duration. The signal was measured using the software LABVIEW (National Instruments, Austin, TX). To see this figure in color, go online.

Flow cytometry

A model No. FC500 analyzer flow cytometer (Beckman Coulter) equipped with CXP ANALYSIS software (Beckman Coulter) was used to perform measurements of nonelectroporated (control) and electroporated cells. Forward-scatter (FS) and side-scatter (SS) measurements were used to distinguish between cells and debris based on cell size and granularity, respectively. After the cell population was gated based on the FS and SS measurements of the control condition (nonpulsed cells), 10,000 events were acquired within the preselected gate for each condition (Fig. 2 *a*). Data was collected for each event with long-pass filters at 525- and 675-nm wavelengths to provide a count of FD^+ and 7-AAD^+ cells, respectively. Before each experiment, spectral compensation was performed due to the overlap of the FD and 7-AAD signals.

Flow cytometry data analysis

The cell population was separated from debris using the FS and SS plot as demonstrated with the circular gate in Fig. 2 *a*. Subsequently, the gated cell population was expanded into a scatter plot of 7-AAD intensity (ordinate)

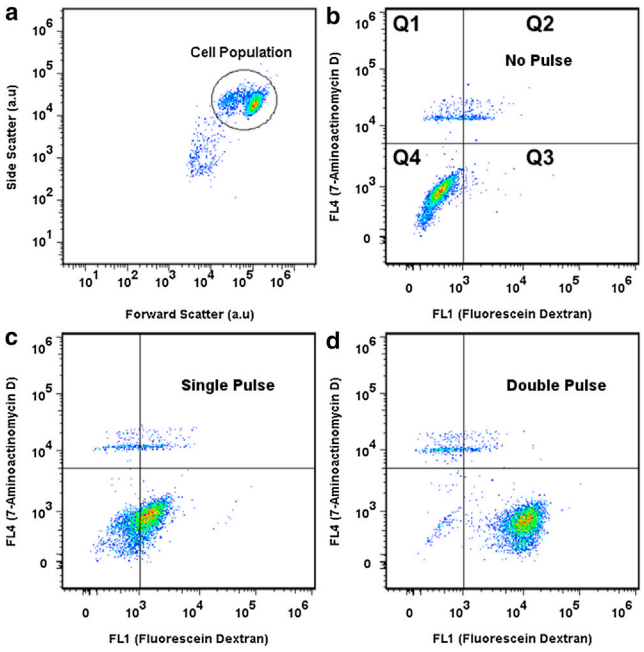

FIGURE 2 Exemplary cell analysis with dot plots. (*a*) Control cells that were not pulsed. These cells are plotted with respect to forward-scatter (abscissa) and side-scatter (ordinate). The cell population in panel *a* is separated from debris using a circular gate. (*b–d*) Abscissa represents the fluorescence signal due to the uptake of Fluorescein-Dextran (FD); the ordinate, 7-Aminoactinomycin D (7-AAD). (*Solid lines*) Separation of the regions of uptake and no-uptake of the respective dyes. Cells in panel *b* are the gated cells from panel *a*, which were not pulsed. Cells in panel *c* received a single pulse of $E_1 = 100{,}000$ V/m and $t_1 = 0.001$ s. Cells in panel *d* received an additional pulse of $E_2 = 30{,}000$ V/m and $t_2 = 0.1$ s with no delay with respect to the first pulse. To see this figure in color, go online.

versus FD intensity (abscissa) (Fig. 2, *b–d*). The FD intensity represents the degree of molecular delivery, whereas 7-AAD represents the presence of a compromised cell membrane any time between 30 min and 2 h postpulsation. These 7-AAD$^+$ cells were presumed to be nonviable.

The limits for the quadrants in the scatter plots were preselected based on the compensation analysis discussed in Flow Cytometry. Therefore, cells in each quadrant represent the following cell populations:

Q1: Dead cells (7-AAD$^+$) that do not contain FD;
Q2: Dead cells (7-AAD$^+$) that contain FD;
Q3: Live Cells (7-AAD$^-$) that contain FD; and
Q4: Live cells (7AAD$^-$) that do not contain FD.

Fig. 2, *b–d*, represents dot plots of cells electroporated with different pulse conditions. Fig. 2 *b* represents control condition with cells that were not pulsed. Fig. 2, *c* and *d*, represents cells after the application of a single and a double pulse, respectively. The majority of the dead cells (7-AAD$^+$) aggregated at a specific fluorescence level for all the experimental conditions, which indicates the saturation of binding sites for 7-AAD within dead cells. The percentage of viable cells (S) was calculated by normalizing the number of cells without 7-AAD fluorescence (Q3+Q4) from the pulsed condition with the same number of cells in the nonpulsed condition.

The vertical line in Fig. 2, *b–d*, separates cells with FD (Q1 and Q2) and without FD (Q3 and Q4). The cells from Fig. 2 *b* were not pulsed, so, essentially, all the cells were void of FD and fell in Q4. The application of a single pulse ($E_1 = 100{,}000$ V/m, $t_1 = 0.001$ s) shifted the cell population partially into Q3, indicating FD delivery (Fig. 2 *c*). The addition of a second pulse, for example, $E_2 = 30{,}000$ V/m and $t_2 = 0.1$ s, as shown in Fig. 2 *d*, pushed the cell population further into Q3, demonstrating enhanced delivery. The efficiency of FD delivery was assessed by identifying the median value of fluorescence intensity (Fig. 3) and determining the increase in intensity relative to a single pulse:

$$NF = \frac{\text{Median (double pulse)} - \text{Median (single pulse)}}{\text{Median (single pulse)}}, \tag{1}$$

where NF denotes normalized fluorescence.

Modeling approach

In addition to flow cytometry measurements, we also used numerical modeling to interpret the trends observed. The model framework combines an asymptotic Smoluchowski equation (ASE) (71) for membrane permeabilization with a Nernst-Planck equation for molecular transport, and the details are presented in our earlier work (15,29,30). Here we summarize the key elements.

Pore nucleation and evolution

The ASE model describing the evolution of the pore statistics follows closely that by Krassowska and Filev (71),

$$\frac{dN}{dt} = q_1 e^{\left(V_m/V_{ep}\right)^2}\left(1 - \frac{N}{N_0 e^{q_2\left(V_m/V_{ep}\right)^2}}\right), \tag{2}$$

$$\frac{dr_j}{dt} = U\left(r_j, V_m, \Gamma\right), \quad j = 1, 2, \cdots, k. \tag{3}$$

Here $N(t,\theta)$ is the local pore number density as a function of time, t, and the polar angle, θ (see Fig. 1 in Li and Lin (30)); N_0, q_1, q_2, and V_{ep} are constants. V_m is the transmembrane potential, r_j is the evolving pore size, U is the advection velocity, and Γ is an effective membrane tension. The subscript j is the index for the pores in a local area element. According to this model, pores nucleate at an initial radius, $r^* = 0.5$ nm, and at a rate described by Eq. 2. They then evolve in size according to Eq. 3 to minimize the total energy of the lipid membrane. Resealing effects are also captured by the ASE. This permeabilization model is coupled to the full electrical problem. Further details as well as relevant parameters are found in Li and Lin (30) and Krassowska and Filev (71), and, for brevity, are not presented here.

FD transport

We adopt a generalized Nernst-Planck system to simulate species transport. In the following, we treat the concentration of FD in a continuum, convective-diffusive framework:

$$\frac{\partial[\mathrm{FD}]}{\partial t} = \nabla\cdot\left(w_{\mathrm{FD}} F z_{\mathrm{FD}}[\mathrm{FD}]\nabla\Phi\right) + \nabla\cdot\left(D_{\mathrm{FD}}\nabla[\mathrm{FD}]\right). \tag{4}$$

Here [FD] denotes the molar concentration of Fluorescein-Dextran, Φ is the electric potential, F is the Faraday constant, z_{FD} is the net charge of FD, D_{FD} is the diffusion coefficient, and w_{FD} is the mechanical mobility (calculated from D_{FD} using Einstein's relation, $D = wRT$, where R is the universal gas constant, and T is temperature). Equation 4 is solved for both the intra- and extracellular spaces, and these are coupled on the membrane by continuity of molar flux density for every species:

$$F_{\mathrm{i,e}} = F_{\mathrm{m}}, \tag{5}$$

where

$$F_{i,e} \equiv -\mathbf{n}\cdot\left(w_{\mathrm{FD}} F z_{\mathrm{FD}}[\mathrm{FD}]\nabla\Phi + D_{\mathrm{FD}}\nabla[\mathrm{FD}]\right)_{i,e}, \tag{6}$$

$$F_m \equiv \rho_p \frac{D_{\mathrm{FD}}(Pe_{\mathrm{FD}} - \ln\gamma)}{h}\frac{(\gamma-1)}{\ln\gamma}\frac{\left([\mathrm{FD}]_e - [\mathrm{FD}]_i\exp(Pe_{\mathrm{FD}})\right)}{(\gamma - \exp(Pe_{\mathrm{FD}}))}. \tag{7}$$

Here $F_{i,e}$ values are the flux densities from the intra- and extracellular spaces, respectively; F_m is the flux density across the membrane; $Pe_{\mathrm{FD}} \equiv w_{\mathrm{FD}} F z_{\mathrm{FD}} V_m / D_{\mathrm{FD}}$ is an effective Péclet number for each species; and $\gamma = \sigma_e/\sigma_i$ the extra/intracellular conductivity. The initial intra- and extracellular

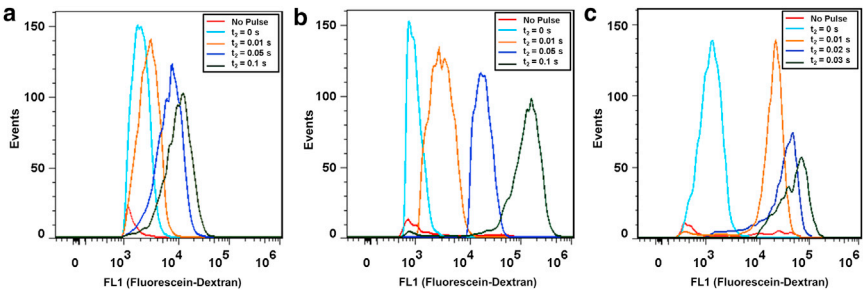

FIGURE 3 Fluorescein-Dextran fluorescence signal for three different second-pulse field strengths at different second-pulse durations. (*a*) $E_2 = 25{,}000$ V/m; (*b*) $E_2 = 50{,}000$ V/m; (*c*) $E_2 = 100{,}000$ V/m. The cell populations of each distribution are obtained from the Q3 quadrant in Fig. 2, *b–d*.To see this figure in color, go online.

FD concentrations are $[FD]_{i,o}$ and $[FD]_{e,o}$, respectively (Table 1, and see the literature (72–75)). The permeabilization result affects the species transport through the pore area density (PAD), ρ_p, in Eq. 7. This quantity is defined by

$$\rho_p(t,\theta) = \sum_{j=1}^{K(t,\theta)} \pi r_j^2/\Delta A, \tag{8}$$

and is calculated for every area element after the pore statistics. Parameters specific to this study are listed in Table 1 and others can be found in Li and Lin (30).

Numerical implementation

The complete model is solved with a finite-volume, alternative-direction implicit scheme in an axisymmetric geometry. The axis of symmetry is aligned with the field direction. A nonuniform spherical grid with higher resolution around the membrane is adopted to optimize computational efficiency. The numerical convergence is tested with respect to resolution by increasing the number of grids.

RESULTS

In this section, we first present data from flow cytometry for all experimental conditions, as well as results from the modeling simulation. A comparison between the two follows. A scaling-relationship-based optimization approach is presented last.

Experimental results

The effects of the second-pulse duration (t_2) and strength (E_2) on the delivery of FD are examined in Fig. 4. Each data point is based on a population of 10,000 cells and is obtained with the analytical method outlined in Flow Cytometry Data Analysis. The normalized fluorescence (*NF*) is calculated according to Eq. 1. Fig. 4 *a* demonstrates that delivery increases linearly with t_2. Fig. 4 *b* shows that *NF* exhibits three regimes with respect to E_2 for all t_2 values. In the first, *NF* increases slowly until E_2 reaches 35,000 V/m, which is followed by a rapid rise between $E_2 =$ 40,000 V/m and $E_2 =$ 60,000 V/m. A plateau is reached for $E_2 >$ 60,000 V/m. To construct a global picture of the system behavior, we use least-square fitting to further process the data. (This method is also practiced below for viability.) The data from Fig. 4 *a* for each constant value of E_2 are first fitted with lines,

$$NF = \alpha(E_2) \times t_2, \tag{9}$$

where α is the slope of each individual line (*solid lines* in Fig. 4 *a*), which corresponds to the delivery rate per unit time. Similarly, in Fig. 4 *b,* the solid lines represent sigmoidal fittings for constant t_2 values and for brevity, the specific forms are not given here. The slope α as obtained from Eq. 9 is plotted as a function of E_2 in Fig. 5. The error bars represent the 95% confidence interval of the linear curve fits in Fig. 4 *a*. The sigmoidal behavior is consistent with the individual curves in Fig. 4 *b*. The dashed lines represent the fitting

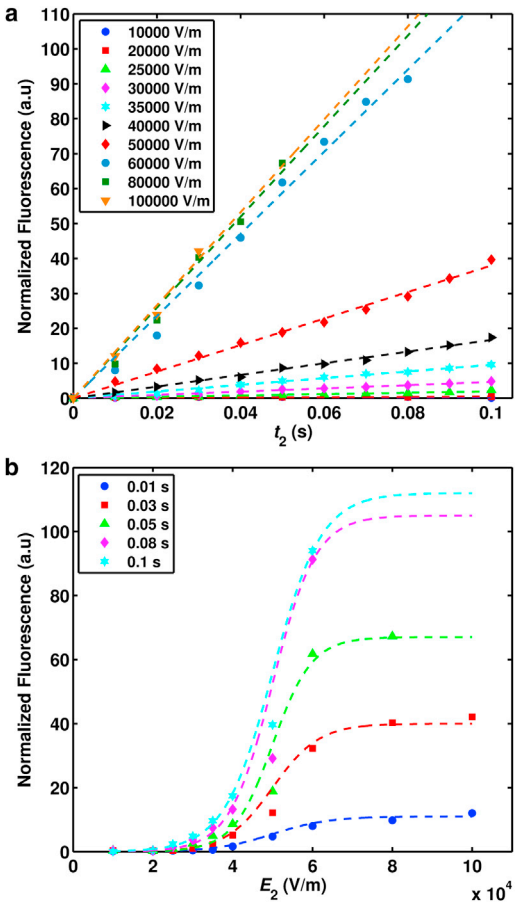

FIGURE 4 (*a* and *b*) The normalized fluorescence (*NF*) of intracellular Fluorescein-Dextran as a result of double-pulse electroporation. (*Symbols*) Experimental data; (*curves*) least-square fitting. For all cases, the first pulse was always $E_1 =$ 100,000 V/m and $t_1 =$ 0.001s. To see this figure in color, go online.

$$\alpha(E_2) = \frac{\alpha_{\max}}{1+\exp\left(\dfrac{E_{2,c}-E_2}{\beta}\right)}, \tag{10}$$

where $\alpha_{\max}$, $E_{2,c}$, and β are fitting constants, and the values can be found in Table 2. Considering Eqs. 10 and 11 together, the entire data set in Fig. 4 *a* can be approximated by the following relation:

$$NF = \frac{\alpha_{\max}}{1+\exp\left(\dfrac{E_{2,c}-E_2}{\beta}\right)} \times t_2. \tag{11}$$

This construction summarizes the whole data trend for delivery.

The effects of the second-pulse parameters on viability (*S*) are presented in Fig. 6. Cells exposed to only a single pulse, the first pulse only, demonstrated the highest *S* at ~97.3%. Similar results were observed by other authors (32,38). For instance, in Puc et al. (32) (in Fig. 2, *c* and *d*), ~90% of cells were permeabilized without affecting

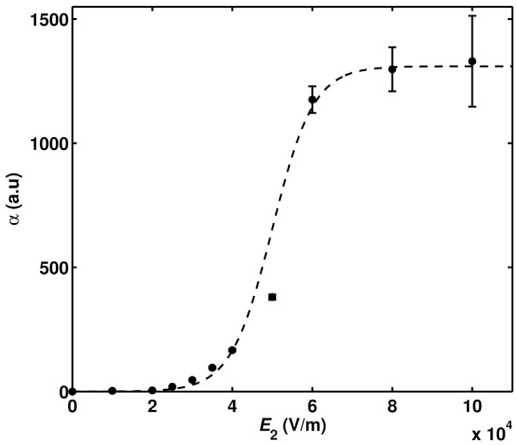

FIGURE 5 The delivery rate per unit time (α, *circles*) as a function of E_2. The value α is extracted from Fig. 4 *a* by calculating the slopes of the linearly fitted lines (Eq. 10), and the error bars represent the 95% confidence interval of the fitting. The correlation between α and E_2 can be further approximated by a least-square sigmoidal fitting (*dashed*). The coefficient of determination is $R^2 = 0.97$.

the overall viability at 1 ms and 1 kV/cm. Viability decreased linearly with increasing t_2 (Fig. 6 *a*) and quadratically with increasing E_2 (Fig. 6 *b*). The solid lines are linear and quadratic fitting for constant E_2 and t_2, respectively. Collectively, the dependence of S on t_2 and E_2 suggests that viability is dependent on the electrical energy ($E_2^2 t_2$). Indeed, as shown in Fig. 7, the relationship between S and $E_2^2 t_2$ is well captured by a straight line with a high coefficient of determination ($R^2 = 0.946$),

$$S\,(\%) = S_0 - \eta E_2^2 t_2, \tag{12}$$

where S_0 and η represent fitting parameters; their values can be found in Table 2.

The scaling relationships (Eqs. 11 and 12 are the basis for an optimization method that will be discussed in the subsection Optimization. Below, we present modeling results to provide basic insights for interpretation of the data trend.

Computational results

In this section, we use the modeling framework outlined in Modeling Approach to simulate both membrane permeabilization and FD transport, such as to correlate with the experimental observations.

TABLE 2 Curve-fitting constants for Eqs. 10–15

Symbol	Value
$\alpha_{f,\max}$	1310 a.u.
$E_{2,c}$	50,000 V/m
β	5156 V/m
S_o	97.3%
η	1.49×10^{-7} m^2%/V^{2}s

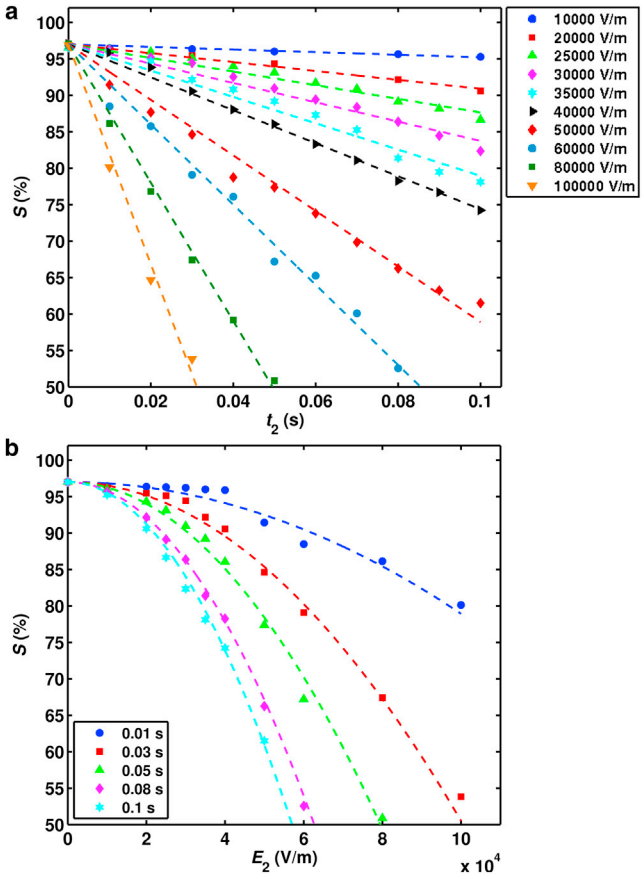

FIGURE 6 The percentage of viable cells after double-pulse electroporation. (*Symbols*) Experimental data; (*curves*) least-square fitting. For all cases, the first pulse was always $E_1 = 100{,}000$ V/m and $t_1 = 0.001$ s. To see this figure in color, go online.

Fig. 8 shows exemplary results on membrane permeabilization. Fig. 8 *a* shows the evolution of the PAD (ρ_p) for $E_2 = 30{,}000$ V/m, and $t_2 = 0.001$ s. Here $\theta = 0$ is facing the

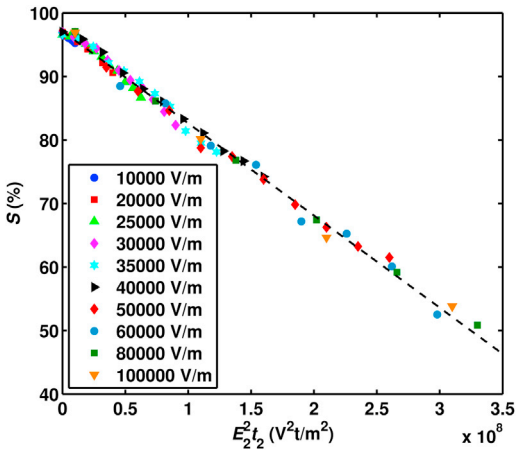

FIGURE 7 Scaling law of viability with respect to the electrical energy ($E_2^2 t_2$). (*Symbols*) Experimental data; (*dashed curve*) least-square fitting given by Eq. 12. Viability decreases linearly with increasing electrical energy. To see this figure in color, go online.

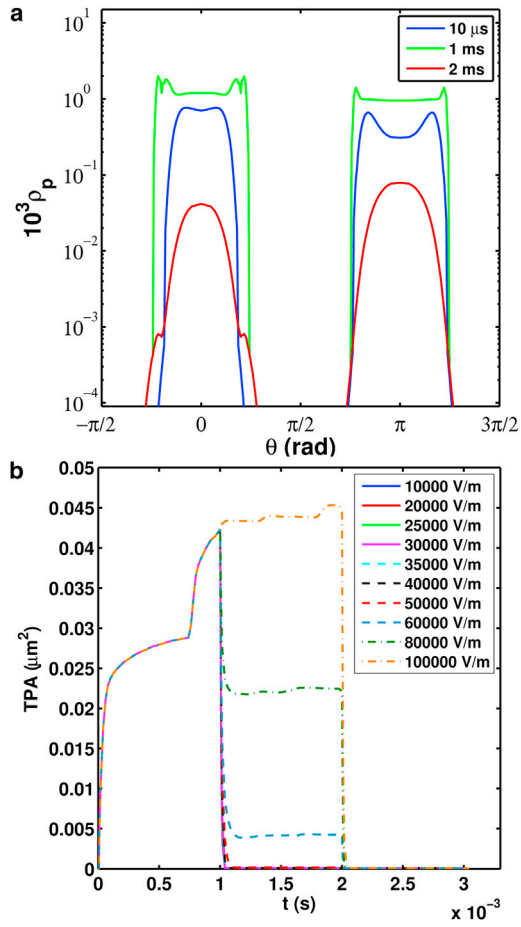

FIGURE 8 (*a*) Polar distribution of the pore area density (PAD). For this case, $E_2 = 30{,}000$ V/m, $t_2 = 0.001$ s, $\theta = 0$ for the cathode-facing pole, from which side most of the negatively charged FD molecules enter. (*b*) The evolution of TPA as a function of time. For all cases, $t_2 = 0.001$ s. To see this figure in color, go online.

cathode pole, and clearly after the first pulse ceases at $t_1 = 0.001$ s, the PAD on both cathode- and anode-facing caps drops to a lower level. This level is strongly correlated with the value of E_2. To characterize the degree of permeabilization, we defined a new quantity, namely, total permeabilized area (TPA),

$$\text{TPA} = \int_0^{2\pi} d\phi \int_0^{\pi/2} \rho_p d\theta, \tag{13}$$

where ϕ is the azimuthal coordinate. Upon considering that the negatively charged FD mainly enters against the direction of the applied field, note the integration with respect to θ is from 0 to $\pi/2$ on the cathode-facing hemisphere only. The evolution of the TPA as a function of time for different E_2 values is shown in Fig. 8 *b*. Upon the application of the second pulse, the TPA appears to adjust rapidly to a new equilibrium value, which is maintained until the end of the pulse. Common to the ASE model, the pores shrink to a value close to $r^* = 0.5$ nm almost immediately postpulsation (24,30). The resulting values for the TPA are ~10^{-4} μm^2 for this postpulsation stage. The trends are similar for other t_2 values that, for the sake of brevity, are not shown here.

Fig. 9 shows the total FD (denoted as TFD) delivered into the single simulated cell for all E_2 and t_2 values studied experimentally. In agreement with the experimental data, the TFD correlates linearly with t_2. Similar to the treatment of the experimental data, we fit TFD as a function of t_2 in Fig. 9 *a* with lines, and the resulting slope (denoted by α_{sim}) is plotted as a function of E_2 in Fig. 9 *b*. Consistent with our experimental work, we observed no significant delivery (per unit time) until E_2 reaches a threshold value. However, note that the threshold value for E_2 is ~25,000 and 50,000 V/m from the experimental and computational results, respectively. Above this value, α_{sim} exhibited a strong and almost linear correlation with E_2 (Fig. 9 *b*). In comparison, we also show the behavior of the TPA in the same figure. For all E_2 values, the value of the TPA is taken at $t = 0.0015$ s, at which time an equilibrium has been established for the second pulse. Theoretically, this equilibrium

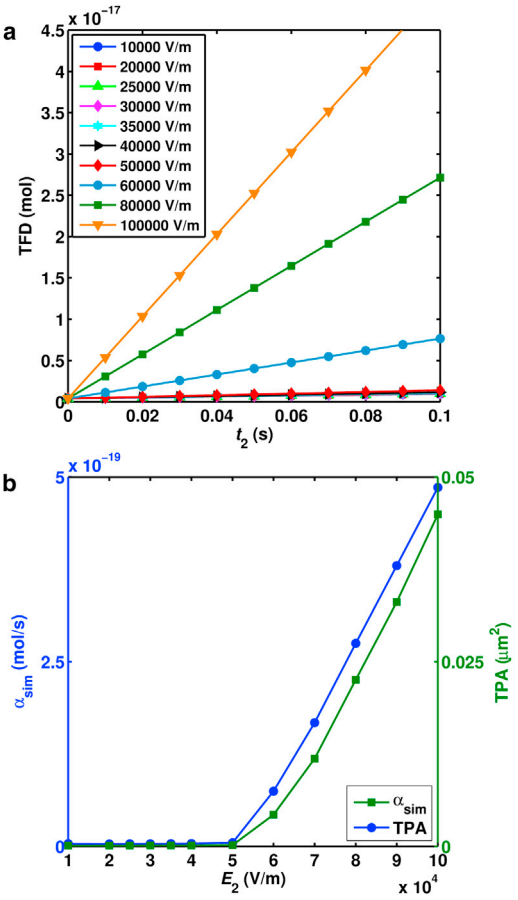

FIGURE 9 (*a*) Simulated results of delivery of total FD (TFD) and (*b*) delivery rate of Dextran (α_{sim}) plotted as a function of t_2 and E_2. To see this figure in color, go online.

value depends only on the strength of the second pulse, and not on the strength or the duration of the first one. The two curves in Fig. 9 *b* share a similar trend.

Comparison between experimental and computational data

In this study, the linear behavior of delivery with respect to t_2 in both the experimental data and the simulations alludes to the dominant role of electrophoretic transport for molecules larger than 4 kDa (25). An exemplary animation of the simulated FD delivery process with a double pulse is included in Movie S1 in the Supporting Material. Although FD does enter the cell via diffusion during and after the pulse application, the contribution is negligibly small per the simulated results. In general, electrophoresis is a fast and active mechanism when compared with diffusion or endocytosis, and is speculated to be the main viable mechanism for molecules >4 kDa (25,30,76).

When compared with the experimental data, the simulation notably captured a critical field above which the delivery with the second pulse becomes effective, although the specific values are different (25,000 and 50,000 V/m, respectively). In this simulation, this critical phenomenon is mediated by that in the pore dynamics. According to the model, when the transmembrane potential is below a threshold value of 0.44 V, pores on the membrane shrink to an equilibrium size of ~1 nm, leading to a weak degree of permeabilization. Theoretically, this threshold value depends only on the energy landscape of the pores, or equivalently, the right-hand side of Eq. 3, and not on the details of the first pulse. Once the threshold is reached, pores expand to a new equilibrium size of ~10 nm. This expansion significantly increases the membrane permeability (reflected in the TPA in Fig. 9), which also allows for appreciable FD electrotransfer. This behavior in pore dynamics is well illustrated by, e.g., Fig. 1 in Neumann (77) (and Fig. 7 in M. Yu and H. Lin, unpublished). However, the discrepancy indicates a necessity for model improvement. Using a simple estimate relating applied field strength and transmembrane potential, the critical value for the latter is estimated to be ~0.22 V for $E_2 = 25{,}000$ V/m (78). This value can be used as a constraint to help revise the energy landscape in the ASE theory.

The simulation also does not capture the plateau in Fig. 5. The cause for this behavior is unknown, and we speculate that it is due to the higher cell-death rate at a field strength approaching 100,000 V/m. During the pulse, a higher field-strength always leads, if only briefly, to higher delivery. However, because FD molecules do not bind within the cell, they may eventually diffuse out of the cell if the membrane remains open for an extended period of time, e.g., in case of cell death. The enhanced delivery therefore does not manifest itself in the data we collected exclusively from Q3 (i.e., live cells only). This effect is not captured by the transport model, which does not include viability predictions.

Optimization

The above studies helped establish the scaling relationships of both delivery and viability with respect to the pulsing parameters. There indeed exists a regime where transport via the second pulse is the most effective. However, to develop an optimization approach, delivery and viability need to be considered in conjunction with each other. The availability of Eqs. 11 and 12 allows us to construct a direct relation between them. We start by specifying a desired viability, e.g., $S = 70\%$. Equation 12 allows us to identify the pulse length t_2 given the field strength E_2:

$$t_2 = \frac{S - S_0}{\eta E_2^2}. \tag{14}$$

Next, this equation is substituted into Eq. 11 to obtain

$$NF = \frac{\alpha_{\max}}{1 + \exp\left(\dfrac{E_{2,c} - E_2}{\beta}\right)} \times \frac{(S - S_0)}{\eta_s E_2^2}. \tag{15}$$

This relation expresses delivery (*NF*) as a function of E_2 and *S*, and is plotted in Fig. 10. For each curve, the viability is kept constant. Therefore, by varying E_2, an optimal field strength can be identified without sacrificing viability. This optimal strength is exactly reached when each constant-viability contour reaches its maximum, which is

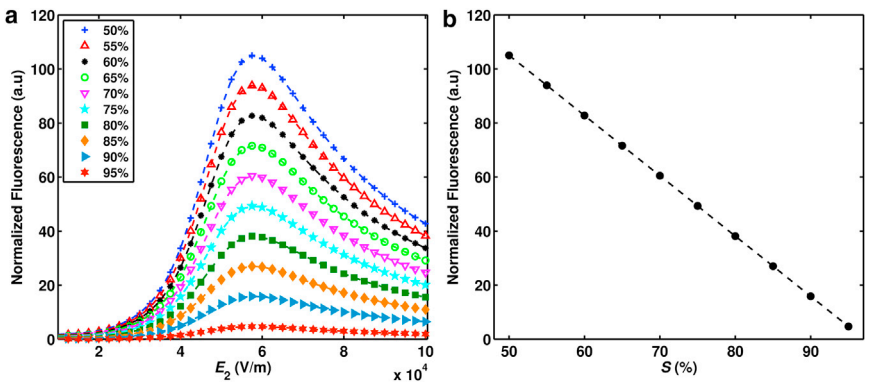

FIGURE 10 *NF* as a function of E_2 and S (Eq. 15). (*a*) The curves can be regarded as constant-viability contours in the phase space of E_2 and *NF*. A maximum value of *NF* is reached at $E_2 =$ 58,000 V/m for all *S* values. (*b*) The maximum value of *NF* for each value of *S* in panel *a*. An inverse linear correlation is observed. To see this figure in color, go online.

consistently at $E_2 = 58{,}000$ V/m. Furthermore, the maximum achievable NF decreases linearly with viability, as shown in Fig. 10 *b*. This result is not surprising, because both NF and S depend linearly on t_2.

Fig. 10 is the main result of this work, which suggests that if the scaling relationships of both delivery and viability with respect to the pulsing parameters can be established, then optimization can systematically pursued. In discussions below, we argue that this approach can be generalized to other cell and other molecule types (32).

DISCUSSION

In our experiments, we used 7-AAD, a molecule that is approximately twice the molecular weight of propidium iodide, to examine membrane integrity and cell viability (79). We believe that this method is a suitable assay for short-term cell death/viability. The dye was added ~30-min postpulsation, and was present in the cell suspension for an average of 2 h until flow cytometry data acquisition (37,38,72). From the literature, the time constant for membrane resealing ranges from seconds to minutes (7,12,13,80,81). Therefore, a cell that is permeant between 30- and 150-min postpulsation will likely remain so permanently (38). In addition, the extended opening of the membrane will significantly perturb the homeostasis of the cell, and will most likely result in necrosis or apoptosis (34,35,82–84). On the other hand, cells that sealed at 30 min may also be at risk of cell death at long-term due to biochemical processes such as nuclear DNA fragmentation, membrane protein denaturation, etc. (38,84). Therefore, the short-term cell-death rate can be regarded as a lower bound for the long-term counterpart (38,83). The relationship between short- and long-term cell viability and membrane permeabilization is a complex one. A full understanding and quantification has yet to be established, which is the scope of future work (37,38,84).

We remark that a similar analysis (using propidium iodide 10-min postpulsation) has been performed by Canatella et al. (37). The study established a qualitative correlation between short-term cell death and the electrical energy. However, the data therein was scattered, and did not exhibit quantitatively a linear correlation as we have presented in this work. We speculate that the difference is caused by the use of decaying instead of square pulses by this earlier work.

In this work, we have selectively investigated the delivery of a single molecular type into a single cell type using HV/LV pulses. Once the target molecule's size and charge, cell type, and pulsing parameters (e.g., HV field strength, duration, and the delay between pulses) change, the scaling relationships may vary accordingly. Nonetheless, we speculate that the data trends observed here assume some generality:

- The sigmoidal dependence on pulse strength for various pulse types corroborates with earlier work, for both small (32,39,85) and large molecules (39,42,48,68), and for different cell types (72). The consistency is not surprising, and attests to the general presence of the lower and upper bounds on delivery as we have previously explained.
- As long as delivery and viability scale differently with the pulsing parameters, an optimal field strength is always identifiable (32,39,42,51,72). For the specific case, presented in Fig. 10, the equiviability contours exhibit a characteristic dome-shape. Curve ascension is attributed to the fact that delivery increases more rapidly than the drop in viability with respect to the field strength; a converse situation leads to the descent. With a change in cell/molecule type, we expect the quantitative details of the curves to vary, but we speculate that the characteristic dome-shape persists.

This work leads to the proposal that similar experiments need to be repeated for a matrix of cell/molecule combinations. The electric field strength and duration of the HV can be tailored with respect to the target molecule to enhance overall performance (see, e.g., Puc et al. (32)). These experiments will each provide answers to the three questions outlined in the Introduction. In addition, further quests can be pursued. For example, Fig. 9 *b* provides an estimate for the critical TMP threshold for effective delivery, which we construe as the threshold for pore expansion. Finding how this value varies with cell type can help build up connections between membrane composition and mechanics. Furthermore, the strong regularity in the relationship between viability and the electrical energy encourages us to further explore similar trends in other cell types. This regularity also suggests that a nonspecific, physical mechanism may be dictating short-term viability, at postpulsation. These efforts help move electroporation-mediated molecular delivery toward a quantitative science.

CONCLUSION

In this work, we performed electroporation experiments to diagnose the effects of HV/LV pulses on delivery and cell viability. The electric pulse was split into two stages without a delay in between: a short, strong pulse to permeabilize the membrane with minimal cell damage, and a second pulse with long duration to extend the electrophoretic transport. The delivery of FD into 3T3 mouse fibroblasts was analyzed with flow cytometry. The main findings, in response to the three questions put forward in the Introduction, are:

1. The LV is much more effective than the HV alone in mediating molecular delivery. The delivery scales linearly with the length of the LV, and exhibits a sigmoidal behavior with respect to its strength. Indeed, according to this behavior, delivery is the most effective for moderate-amplitude electric fields.
2. Viability exhibits a convincing linear correlation with the electrical energy. The strong regularity in the data trend is a main contribution of this work.

3. The different yet well-defined scaling relationships of delivery and viability on the pulsing parameters ensure that optimal field strength can be identified to achieve maximum delivery without compromising viability.

We have also employed a whole-cell level model to predict permeabilization and delivery. A direct comparison between the experimental and numerical results elucidates underlying mechanisms governing the system behavior. The model prediction corroborates the linearity between delivery and the second-pulse duration. The existence of a threshold TMP value for effective delivery with the second pulse is related to a sudden expansion in the equilibrium pore size at that critical point. Although the data trends in this study are observed for a single cell/molecule combination, we speculate that the qualitative behavior persist for other configurations. Together, our efforts establish a route for protocol optimization: Targeted optimization is only possible when both the scaling behavior for delivery and viability are quantified, and can be predicted. This work is, to our knowledge, the first step toward moving electroporation-mediated molecular delivery to a predictable technique.

SUPPORTING MATERIAL

One movie is available at http://www.biophysj.org/biophysj/supplemental/S0006-3495(14)00071-X.

REFERENCES

1. André, F., and L. M. Mir. 2004. DNA electrotransfer: its principles and an updated review of its therapeutic applications. *Gene Ther.* 11 (*Suppl 1*):S33–S42.
2. Gehl, J., T. Skovsgaard, and L. M. Mir. 1998. Enhancement of cytotoxicity by electropermeabilization: an improved method for screening drugs. *Anticancer Drugs.* 9:319–325.
3. Heller, R., S. Shirley, …, L. Heller. 2011. Electroporation based gene therapy—from the bench to the bedside. *In* Annual International Conference of the IEEE Engineering in Medicine and Biology Society IEEE, New York, pp. 736–738.
4. Teissié, J., J. M. Escoffre, …, M. Golzio. 2012. Drug delivery by electropulsation: recent developments in oncology. *Int. J. Pharm.* 423:3–6.
5. Weaver, J. C., K. C. Smith, …, T. R. Gowrishankar. 2012. A brief overview of electroporation pulse strength-duration space: a region where additional intracellular effects are expected. *Bioelectrochemistry.* 87:236–243.
6. Costa, M., M. Dottori, …, E. G. Stanley. 2007. A method for genetic modification of human embryonic stem cells using electroporation. *Nat. Protoc.* 2:792–796.
7. Escoffre, J. M., T. Portet, …, M. P. Rols. 2009. What is (still not) known of the mechanism by which electroporation mediates gene transfer and expression in cells and tissues. *Mol. Biotechnol.* 41:286–295.
8. Fantozzi, F., E. Arturoni, and R. Barbucci. 2010. The effects of the electric fields on hydrogels to achieve antitumoral drug release. *Bioelectrochemistry.* 78:191–195.
9. Larkin, J. O., C. G. Collins, …, G. C. O'Sullivan. 2007. Electrochemotherapy: aspects of preclinical development and early clinical experience. *Ann. Surg.* 245:469–479.
10. Chen, C., S. W. Smye, …, J. A. Evans. 2006. Membrane electroporation theories: a review. *Med. Biol. Eng. Comput.* 44:5–14.
11. Kandušer, M., and D. Miklavčič. 2009. Electroporation in Biological Cell and Tissue: An Overview. Electrotechnologies for Extraction from Food Plants and Biomaterials Series. Springer, New York, pp. 1–37.
12. Teissié, J., M. Golzio, and M. P. Rols. 2005. Mechanisms of cell membrane electropermeabilization: a minireview of our present (lack of?) knowledge. *Biochim. Biophys. Acta.* 1724:270–280.
13. Weaver, J. C., and Y. A. Chizmadazhev. 1996. Theory of electroporation: a review. *Bioelectrochem. Bioenerg.* 41:135–160.
14. Ivorra, A., J. Villemejane, and L. M. Mir. 2010. Electrical modeling of the influence of medium conductivity on electroporation. *Phys. Chem. Chem. Phys.* 12:10055–10064.
15. Li, J., and H. Lin. 2010. The current-voltage relation for electropores with conductivity gradients. *Biomicrofluidics.* 4:13206.
16. Kotnik, T., G. Pucihar, …, L. Mir. 2003. Role of pulse shape in cell membrane electropermeabilization. *Biochim. Biophys. Acta Biomembr.* 1614:193–200.
17. Pucihar, G., L. M. Mir, and D. Miklavčič. 2002. The effect of pulse repetition frequency on the uptake into electropermeabilized cells in vitro with possible applications in electrochemotherapy. *Bioelectrochemistry.* 57:167–172.
18. Pucihar, G., T. Kotnik, …, D. Miklavčič. 2001. The influence of medium conductivity on electropermeabilization and survival of cells in vitro. *Bioelectrochemistry.* 54:107–115.
19. Neu, J. C., and W. Krassowska. 1999. Asymptotic model of electroporation. *Phys. Rev. E Stat. Phys. Plasmas Fluids Relat. Interdiscip. Topics.* 59:3471–3482.
20. Neu, J. C., and W. Krassowska. 2003. Modeling postshock evolution of large electropores. *Phys. Rev. E Stat. Nonlin. Soft Matter Phys.* 67:021915.
21. Neu, J. C., K. C. Smith, and W. Krassowska. 2003. Electrical energy required to form large conducting pores. *Bioelectrochemistry.* 60:107–114.
22. Neu, J. C., and W. Krassowska. 2006. Singular perturbation analysis of the pore creation transient. *Phys. Rev. E Stat. Nonlin. Soft Matter Phys.* 74:031917.
23. Tsong, T. Y. 1991. Electroporation of cell membranes. *Biophys. J.* 60:297–306.
24. Smith, K. C., J. C. Neu, and W. Krassowska. 2004. Model of creation and evolution of stable electropores for DNA delivery. *Biophys. J.* 86:2813–2826.
25. Rols, M. P., and J. Teissié. 1998. Electropermeabilization of mammalian cells to macromolecules: control by pulse duration. *Biophys. J.* 75:1415–1423.
26. Neumann, E., M. Schaefer-Ridder, …, P. H. Hofschneider. 1982. Gene transfer into mouse lyoma cells by electroporation in high electric fields. *EMBO J.* 1:841–845.
27. Sukharev, S. I., V. A. Klenchin, …, Y. A. Chizmadazhev. 1992. Electroporation and electrophoretic DNA transfer into cells. The effect of DNA interaction with electropores. *Biophys. J.* 63:1320–1327.
28. Djuzenova, C. S., U. Zimmermann, …, G. Fuhr. 1996. Effect of medium conductivity and composition on the uptake of propidium iodide into electropermeabilized myeloma cells. *Biochim. Biophys. Acta.* 1284:143–152.
29. Li, J., W. Tan, …, H. Lin. 2013. The effect of extracellular conductivity on electroporation-mediated molecular delivery. *Biochim. Biophys. Acta Biomembr.* 1828:461–470.
30. Li, J., and H. Lin. 2011. Numerical simulation of molecular uptake via electroporation. *Bioelectrochemistry.* 82:10–21.
31. Müller, K. J., V. L. Sukhorukov, and U. Zimmermann. 2001. Reversible electropermeabilization of mammalian cells by high-intensity, ultrashort pulses of submicrosecond duration. *J. Membr. Biol.* 184:161–170.

32. Puc, M., T. Kotnik, …, D. Miklavčič. 2003. Quantitative model of small molecules uptake after in vitro cell electropermeabilization. *Bioelectrochemistry.* 60:1–10.

33. Sadik, M. M., J. Li, …, H. Lin. 2013. Quantification of propidium iodide delivery using millisecond electric pulses: experiments. *Biochim. Biophys. Acta Biomembr.* 1828:1322–1328.

34. Beebe, S. J., P. M. Fox, …, K. H. Schoenbach. 2002. Nanosecond pulsed electric field (nsPEF) effects on cells and tissues: apoptosis induction and tumor growth inhibition. *IEEE Trans. Plasma Sci.* 30:286–292.

35. Beebe, S. J., P. M. Fox, …, K. H. Schoenbach. 2003. Nanosecond, high-intensity pulsed electric fields induce apoptosis in human cells. *FASEB J.* 17:1493–1495.

36. Buescher, E. S., and K. H. Schoenbach. 2003. Effects of submicrosecond, high intensity pulsed electric fields on living cells—intracellular electromanipulation. *IEEE Trans. Dielectr. Electr. Insul.* 10:788–794.

37. Canatella, P. J., J. F. Karr, …, M. R. Prausnitz. 2001. Quantitative study of electroporation-mediated molecular uptake and cell viability. *Biophys. J.* 80:755–764.

38. Gabriel, B., and J. Teissié. 1995. Control by electrical parameters of short- and long-term cell death resulting from electropermeabilization of Chinese hamster ovary cells. *Biochim. Biophys. Acta.* 1266:171–178.

39. He, H., D. C. Chang, and Y. K. Lee. 2007. Using a micro electroporation chip to determine the optimal physical parameters in the uptake of biomolecules in HeLa cells. *Bioelectrochemistry.* 70:363–368.

40. Joshi, R. P., Q. Hu, …, S. J. Beebe. 2002. Simulations of electroporation dynamics and shape deformations in biological cells subjected to high voltage pulses. *IEEE Trans. Plasma Sci.* 30:1536–1546.

41. Moore, J. C., K. Atze, …, R. P. Hart. 2010. Efficient, high-throughput transfection of human embryonic stem cells. *Stem Cell Res. Ther.* 1:23.

42. Neumann, E., S. Kakorin, …, T. Tomov. 1996. Calcium-mediated DNA adsorption to yeast cells and kinetics of cell transformation by electroporation. *Biophys. J.* 71:868–877.

43. Richard, I., M. Ader, …, U. Bartsch. 2005. Electroporation-based gene transfer for efficient transfection of neural precursor cells. *Brain Res. Mol. Brain Res.* 138:182–190.

44. Faurie, C., E. Phez, …, M. Rols. 2004. Effect of electric field vectoriality on electrically mediated gene delivery in mammalian cells. *Biochim. Biophys. Acta Biomembr.* 1665:92–100.

45. Kotnik, T., D. Miklavčič, and L. M. Mir. 2001. Cell membrane electropermeabilization by symmetrical bipolar rectangular pulses. Part II. Reduced electrolytic contamination. *Bioelectrochemistry.* 54:91–95.

46. Miklavčič, D., and L. Towhidi. 2010. Numerical study of the electroporation pulse shape effect on molecular uptake of biological cells. *Radiol.Oncol.* 44:34–41.

47. Prausnitz, M. R., J. D. Corbett, …, J. C. Weaver. 1995. Millisecond measurement of transport during and after an electroporation pulse. *Biophys. J.* 68:1864–1870.

48. Prausnitz, M. R., B. S. Lau, …, J. C. Weaver. 1993. A quantitative study of electroporation showing a plateau in net molecular transport. *Biophys. J.* 65:414–422.

49. Rols, M. P., and J. Teissié. 1990. Electropermeabilization of mammalian cells. Quantitative analysis of the phenomenon. *Biophys. J.* 58:1089–1098.

50. Zaharoff, D. A., J. W. Henshaw, …, F. Yuan. 2008. Mechanistic analysis of electroporation-induced cellular uptake of macromolecules. *Exp. Biol. Med. (Maywood).* 233:94–105.

51. Rols, M. P., and J. Teissié. 1989. Ionic-strength modulation of electrically induced permeabilization and associated fusion of mammalian cells. *Eur. J. Biochem.* 179:109–115.

52. Barrau, C., J. Teissié, and B. Gabriel. 2004. Osmotically induced membrane tension facilitates the triggering of living cell electropermeabilization. *Bioelectrochemistry.* 63:327–332.

53. Wang, H. Y., and C. Lu. 2006. High-throughput and real-time study of single cell electroporation using microfluidics: effects of medium osmolarity. *Biotechnol. Bioeng.* 95:1116–1125.

54. Golzio, M., M. P. Mora, …, M. P. Rols. 1998. Control by osmotic pressure of voltage-induced permeabilization and gene transfer in mammalian cells. *Biophys. J.* 74:3015–3022.

55. Klenchin, V. A., S. I. Sukharev, …, Y. A. Chizmadzhev. 1991. Electrically induced DNA uptake by cells is a fast process involving DNA electrophoresis. *Biophys. J.* 60:804–811.

56. Pliquett, U., E. A. Gift, and J. C. Weaver. 1996. Determination of the electric field and anomalous heating caused by exponential pulses with aluminum electrodes in electroporation experiments. *Bioelectrochem. Bioenerg.* 39:39–53.

57. Saulis, G., R. Lapé, …, D. Mickevicius. 2005. Changes of the solution pH due to exposure by high-voltage electric pulses. *Bioelectrochemistry.* 67:101–108.

58. Fox, M. B., D. C. Esveld, …, R. M. Boom. 2006. Electroporation of cells in microfluidic devices: a review. *Anal. Bioanal. Chem.* 385:474–485.

59. Lee, E. S., D. Robinson, …, R. V. Davalos. 2006. Microfluidic electroporation of robust 10-micrometer vesicles for manipulation of picoliter volumes. *Bioelectrochemistry.* 69:117–125.

60. Lu, H., M. A. Schmidt, and K. F. Jensen. 2005. A microfluidic electroporation device for cell lysis. *Lab Chip.* 5:23–29.

61. Movahed, S., and D. Li. 2013. A theoretical study of single-cell electroporation in a microchannel. *J. Membr. Biol.* 246:151–160.

62. Stroh, T., U. Erben, …, B. Siegmund. 2010. Combined pulse electroporation—a novel strategy for highly efficient transfection of human and mouse cells. *PLoS ONE.* 5:e9488.

63. Wolf, H., M. P. Rols, …, J. Teissié. 1994. Control by pulse parameters of electric field-mediated gene transfer in mammalian cells. *Biophys. J.* 66:524–531.

64. Zhan, Y., Z. Cao, …, C. Lu. 2012. Low-frequency ac electroporation shows strong frequency dependence and yields comparable transfection results to dc electroporation. *J. Control. Release.* 160:570–576.

65. Kandušer, M., D. Miklavčič, and M. Pavlin. 2009. Mechanisms involved in gene electrotransfer using high- and low-voltage pulses—an in vitro study. *Bioelectrochemistry.* 74:265–271.

66. André, F. M., J. Gehl, …, L. M. Mir. 2008. Efficiency of high- and low-voltage pulse combinations for gene electrotransfer in muscle, liver, tumor, and skin. *Hum. Gene Ther.* 19:1261–1271.

67. Pucihar, G., J. Krmelj, …, D. Miklavčič. 2011. Equivalent pulse parameters for electroporation. *IEEE Trans. Biomed. Eng.* 58:3279–3288.

68. Bureau, M. F., J. Gehl, …, D. Scherman. 2000. Importance of association between permeabilization and electrophoretic forces for intramuscular DNA electrotransfer. *Biochim. Biophys. Acta.* 1474:353–359.

69. Cukjati, D., D. Batiuskaite, …, L. M. Mir. 2007. Real time electroporation control for accurate and safe in vivo non-viral gene therapy. *Bioelectrochemistry.* 70:501–507.

70. Prausnitz, M. R., V. G. Bose, …, J. C. Weaver. 1993. Electroporation of mammalian skin: a mechanism to enhance transdermal drug delivery. *Proc. Natl. Acad. Sci. USA.* 90:10504–10508.

71. Krassowska, W., and P. D. Filev. 2007. Modeling electroporation in a single cell. *Biophys. J.* 92:404–417.

72. Kandušer, M., M. Sentjurc, and D. Miklavčič. 2006. Cell membrane fluidity related to electroporation and resealing. *Eur. Biophys. J.* 35:196–204.

73. Berk, D. A., F. Yuan, …, R. K. Jain. 1993. Fluorescence photobleaching with spatial Fourier analysis: measurement of diffusion in light-scattering media. *Biophys. J.* 65:2428–2436.

74. Granath, K. A., and B. E. Kvist. 1967. Molecular weight distribution analysis by gel chromatography on Sephadex. *J. Chromatogr. A.* 28:69–81.

75. Luby-Phelps, K., P. E. Castle, …, F. Lanni. 1987. Hindered diffusion of inert tracer particles in the cytoplasm of mouse 3T3 cells. *Proc. Natl. Acad. Sci. USA*. 84:4910–4913.

76. Weaver, J. C. 2000. Electroporation of cells and tissues. *IEEE Trans. Plasma Sci.* 28:24–33.

77. Neumann, E. 1992. Membrane electroporation and direct gene transfer. *Bioelectrochem. Bioenerg.* 28:247–267.

78. Yu, M., and H. Lin. 2013. Quantification of propidium iodide delivery with millisecond electric pulses: a model study. Preprint, submitted January 27, 2014. http://arxiv.org/abs/1401.6954.

79. Zhao, Y., Z. Zheng, …, R. A. Morgan. 2006. High-efficiency transfection of primary human and mouse T lymphocytes using RNA electroporation. *Mol. Ther.* 13:151–159.

80. He, H., D. C. Chang, and Y.-K. Lee. 2008. Nonlinear current response of micro electroporation and resealing dynamics for human cancer cells. *Bioelectrochemistry.* 72:161–168.

81. Khine, M., C. Ionescu-Zanetti, …, L. P. Lee. 2007. Single-cell electroporation arrays with real-time monitoring and feedback control. *Lab Chip*. 7:457–462.

82. Hofmann, F., H. Ohnimus, …, C. Jassoy. 1999. Electric field pulses can induce apoptosis. *J. Membr. Biol.* 169:103–109.

83. Piñero, J., M. López-Baena, …, F. Cortés. 1997. Apoptotic and necrotic cell death are both induced by electroporation in HL60 human promyeloid leukemia cells. *Apoptosis.* 2:330–336.

84. Lee, R. C. 2005. Cell injury by electric forces. *Ann. N. Y. Acad. Sci.* 1066:85–91.

85. Venslauskas, M. S., S. Satkauskas, and R. Rodaite-Riseviciene. 2010. Efficiency of the delivery of small charged molecules into cells in vitro. *Bioelectrochemistry.* 79:130–135.